Supporting Information

Two-Photon-Excited Ultralong Organic Room Temperature Phosphorescence by Operating Dual-Channel Triplet Harvesting

Zhu Mao, Zhan Yang, Chao Xu, Zongliang Xie, Long Jiang, Feng Long Gu, Juan Zhao,* Yi Zhang, Matthew P. Aldred, and Zhenguo Chi

Experimental Procedures

Chemical Reagents and Materials

The reagents and solvents were purchased from commercial sources. 2-Bromobenzaldehyde, phenylmagnesium bromide, pyridium chlorochromate (PCC) and carbazole were purchased from J&K and were used directly without any further purification. The solvents ethanol, tetrahydrofuran (THF) and dimethylformamide (DMF) were purchased from Guangzhou chemical reagents factory.

General Information

The ^{1}H and ^{13}C spectra were recorded on a Bruker AVANCE 400 spectrometer ((400 MHz)) in DMSO-d_6 and $CDCl_3$, respectively. The mass spectra were obtained on thermospectrometers (DSQ & MAT95XP-HRMS). Differential scanning calorimetry (DSC) was carried out using the NETZSCH DSC 204 F1 instrument with a heating rate of 10 K/min in a pure nitrogen flow. High-performance liquid chromatography (HPLC) was measured by a Thremo LCQ DECA XP liquid chromatography spectrometry. UV-visible absorption spectra of solutions and solid were performed on Hitachi U-3900 and Shimadzu UV3600 ultraviolet-visible-near-infrared (UV-Vis-NIR) spectrometer, respectively. Steady-state photoluminescence spectra, excitation-emission-matrix spectra, transient decay spectra and photoluminescence quantum yield (PLQY) were carried out using a Jobin Yvon-Horiba FL-3 spectrofluorometer and equipped with a calibrated integrating sphere. Phosphorescence spectra, temperature-dependent phosphorescence spectra, and temperature-dependent decay curves were obtained through Ocean Optics QE65 Pro CCD integrated with Corning heater and Ocean Optics LED-365 or LED-405 as excitation sources. CIE coordinates were calculated by CIE 1931 Chromaticity coordinated calculator (version 1.6.0.2) based on the delayed spectrum. Excitation-energy-dependent steady-state spectra were recorded with Ocean Optics QE65 Pro CCD and excited with Continuum Minilite YAG laser (repetition rate of 15 Hz). The afterglow photographs were recorded with a Canon EOS 550D Camera.

Synthesis of compound *o*-Cz

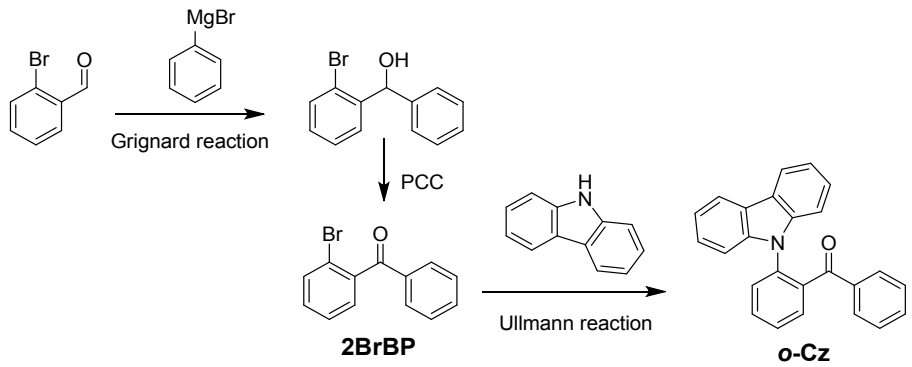

Figure S1. The synthetic route for compound ***o*-Cz**.

Procedure for the synthesis of *(2-(9H-carbazol-9-yl)phenyl)(phenyl)methanone* (*o*-Cz)

Synthesis of ***o*-Cz**. The intermediate compound 2BrBP was synthesized according to the previous work.[1] ^{1}H NMR data of ***o*-Cz** recorded in (DMSO-d_6, 400 MHz) : δ 8.00–7.92 (m, 2H), 7.88 (td, 1H, J = 7.5 Hz), 7.80 (dd, 1H, J = 7.7 Hz), 7.74 (td, 1H, J = 7.5 Hz), 7.67 (d, 1H, J = 7.8Hz), 7.30 (dd, 2H, J = 8.3 Hz), 7.23–7.08 (m, 7H), 6.95 (dd, 2H, J = 8.4). ^{13}C NMR ($CDCl_3$,126 MHz): δ 96.74, 140.90, 137.70, 136.47, 136.18, 132.51, 131.89, 131.20, 128.89, 128.29, 127.79, 126.90, 125.71, 123.20, 119.93, 119.88, 109.98, 109.90. EI-MS m/z: $[m]^+$ cald for $C_{25}H_{17}NO$, 347, found 347. HRMS m/z: $[m]^+$ calcd for $C_{25}H_{17}NO$, 347.1310, found 347.1307.

The X-ray crystal structure of *o*-Cz

The single crystal was obtained by slow evaporation of a mixed solvent (DCM and ethanol (2:1)), and the X-ray diffraction data was collected from the instrument Agilent Technologies Gemini A Ultra system with Cu-Kα

radiation (λ = 1.54178 Å) at 275(6) K and resolved using direct methods with OLEX2. The CCDC number of ***o*-Cz** is 1885292.

Table S1. Crystal data and structure refinement for ***o*-Cz**.

Empirical formula	C25 H17 N O
Formula weight	347.39
Temperature	275(6) K
Wavelength	1.54184 Å
Crystal system	Monoclinic
Space group	$P2_1/c$
Unit cell dimensions	a = 11.5634(2) Å alpha = 90 deg.
	b = 15.7484(2) Å beta = 96.1930(10) deg.
	c = 10.0607(2) Å gamma = 90 deg.
Volume	1821.41(5) $Å^3$
Z	4
Density (calculated)	1.267 mg/m^3
Absorption coefficient	0.601 mm^{-1}
F(000)	728.0
Crystal size	0.20 x 0.20 x 0.40 mm^3
Theta range for data collection	7.69 to 148.344
Index ranges	-14<=h<=11, -19<=k<=17, -12<=l<=10
Reflections collected	11841
Independent reflections	3644 [Rint = 0.0214, Rsigma = 0.0159]
Max. and min. transmission	1.000 and 0.906
Data / restraints / parameters	3644/0/245
Goodness-of-fit on F^2	1.057
Final R indices [I>2sigma(I)]	R_1 = 0.0390, wR_2 = 0.1168
R indices (all data)	R_1 = 0.0417, wR_2 = 0.1203
Largest diff. peak and hole	0.15 and -0.13 e.$Å^{-3}$

Theoretical calculations

Molecular geometries were extracted in single crystals and performed by Gaussian 09W program package with time-dependent density functional theory (TD-DFT) with Beck's three-parameter hybrid exchange functional[2] and Lee, and Yang and Parr correlation functional[3] (B3LYP) with 6-31G* basic set. Energy level distribution of the isolated molecules simulated in THF solutions with a cavity of a THF solvent and using the polarizable continuum model. Natural transition orbital (NTO) analysis was extracted based on TD-DFT results and visualized via Gaussview (6.0.16). Spin-orbital couplings (SOC) matrix elements were calculated via the Beijing Density Functional (BDF) program based on B3LYP/6-31G*.[4] Non-covalent interactions (NCI) of intramolecular and intermolecular interactions analyses were carried out by Multiwfn[5] with reduced density gradient (RDG) and independent gradient model (IGM), respectively.[6] The NCI results were plotted via VMD software (version 1.9.3).[7]

The calculations of the second hyperpolarizabilities

The TPA process corresponds to simultaneous absorption of two photons. During this process, the TPA efficiency can be characterized by the TPA cross section $\delta(\omega)$ at optical frequency $\omega/2\pi$, and it can be directly related to the imaginary part of the third-order hyperpolarizability $\gamma(-\omega;\omega,-\omega,\omega)$, as shown in equation 1

$$\delta(\omega) = \frac{4\pi^2}{\hbar n^2 c^2} L^4 (\hbar\omega)^2 \mathrm{Im}[\gamma(-\omega;\omega,-\omega,\omega)] \quad (1)$$

where $\hbar\omega$ is the energy of the incoming photons, n denotes the refractive index of the medium, and L corresponds to the localfield factor.

Employing the perturbation theory and the density matrix method, the sum-over-states (SOS) expression can be deduced to evaluate the components of the second hyperpolarizability. The SOS equation for second hyperpolarizability γ is

$$\gamma_{ijkl}(-\omega;\omega,-\omega,\omega) = \frac{1}{6}P(i,j,k,l;-\omega,\omega,-\omega,\omega) \times \sum_{m\neq g}\sum_{n\neq g}\sum_{p\neq g} \frac{\langle g|\mu_i|m\rangle\langle m|\mu_j|n\rangle\langle n|\mu_k|p\rangle\langle p|\mu_l|g\rangle}{(E_m-\hbar\omega-i\Gamma_m)(E_n-i\Gamma_n)(E_p-\hbar\omega-i\Gamma_p)} - \sum_{m\neq g}\sum_{n\neq g} \frac{\langle g|\mu_i|m\rangle\langle m|\mu_j|g\rangle\langle g|\mu_k|n\rangle\langle n|\mu_l|g\rangle}{(E_m-\hbar\omega-i\Gamma_m)(E_n-\hbar\omega-i\Gamma_n)(E_n+i\Gamma_n)} \quad (2)$$

where g, m, n, and p denote the ground state and excited states; $|m\rangle$ is an electronic wave function with energy $\hbar\omega$ relative to the ground electronic state; μ_i is the α_{th}(=x, y, z) component of the dipole operator. Γ_m is the damping factor of excited-state m.[5, 8-9]

In the present work, all damping factors Γ are set to 0.10 eV. A chosen basis set size of 280 states included in both configuration interaction and SOS expansion is sufficient for convergence for γ of all the molecules. According to the above formula, the second hyperpolarizabilities γ of ***p*-Cz** and ***o*-Cz** include the contributions from 280 lowest-lying excited states are calculated by modified Multiwfn program are 411.90 × 10^{-36} esu and 6022.53 × 10^{-36} esu, respectively. Thus, the results indicate that ***o*-Cz** has larger TPA cross sections and it is a promising candidate for TPA molecule.

Two-photon induced emission measurements

Two-photon induced emission and intensity-dependent emission spectra were collected at 90° relative to the excitation laser and performed on Princeton Instruments PIXIS400 CCD equipped with Princeton Instrument IsoPlane 160 as monochrometer and Spectra-Physics ultrafast OPO as femtosecond laser excitation source. Two-photon induced phosphorescence were excited by an ultrafast amplified Ti: Sapphire laser with a central wavelength of 808 nm, a pulse length of 95 fs and a repetition rate of 1 kHz. The corresponding spectra and decay curve were recorded by Ocean Optics QE65 Pro CCD with an integral time of 8 ms. The two-photon induced decay lifetime was fitted by Origin. All the above measurements were carried out under ambient conditions. The difference of the two-photon induced steady-state spectral profiles and lifetime compared with the one-photon induced emission is ascribed to the different spectrophotometers used.

Photophysical properties

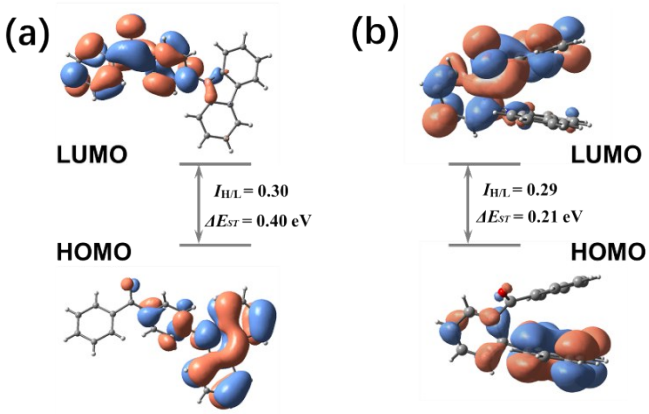

Figure S2. The overlap integral of the norm ($I_{H/L}$) and the lowest singlet-triplet energy gap (ΔE_{ST}) of the HOMO and LUMO for (a) ***p*-Cz** and (b) ***o*-Cz**. The geometries are extracted from single crystals analysis.

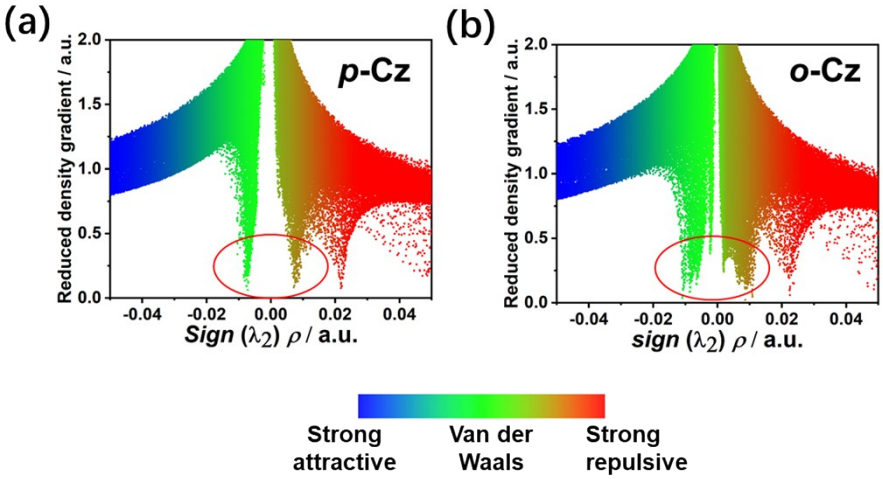

Figure S3. Plots of the reduced density gradient (RDG) with isovalue of 0.5 versus the electron density of (a) ***p*-Cz** and (b) ***o*-Cz**. The geometries are extracted from single crystal x-ray diffraction analysis.

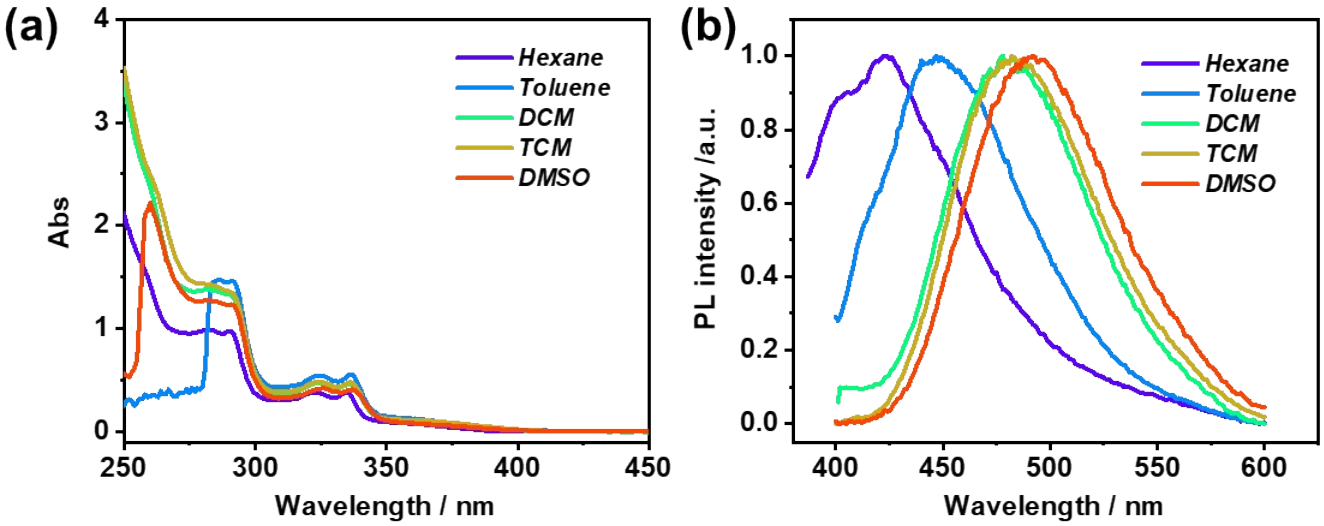

Figure S4. Solvatochromism of ***o*-Cz** in dilute solutions (1×10^{-5} M). (a) UV-Vis absorption spectra and (b) PL spectra, in different polarity solvents.

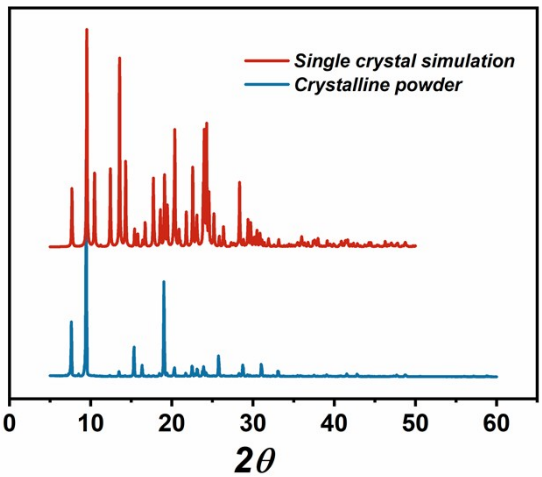

Figure S5. Powder X-ray diffraction and single crystal simulation diffraction of ***o*-Cz**.

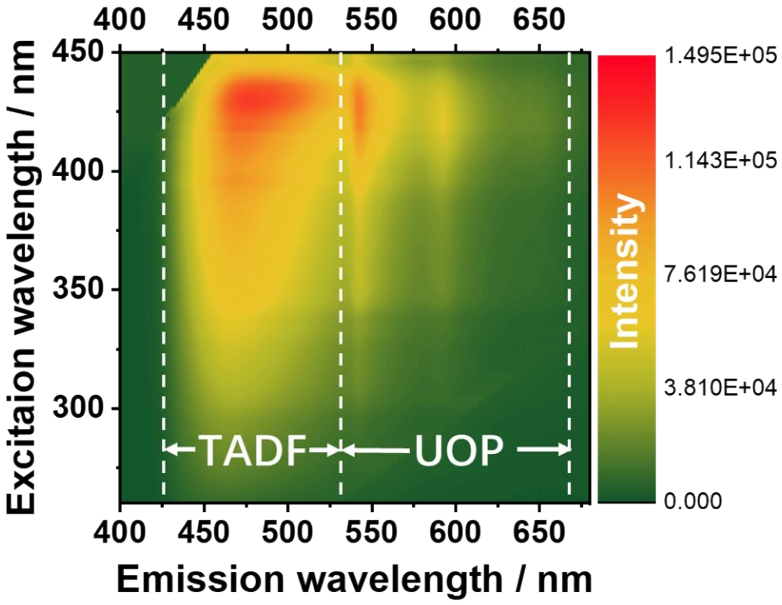

Figure S6. Excitation-emission-matrix spectra of ***o*-Cz** in the solid-state under ambient conditions. Emission intensity enhances with the color changing from green to yellow and to red.

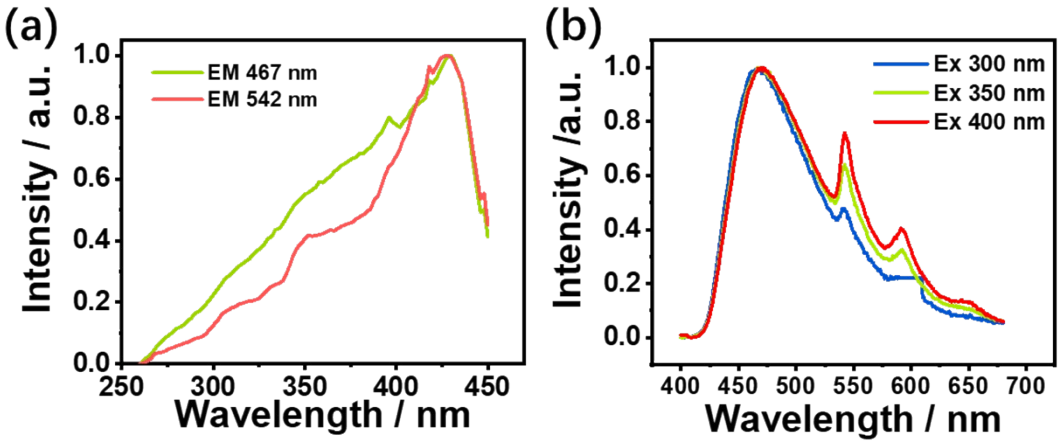

Figure S7. (a) Normalized excitation spectra of ***o*-Cz** in the solid-state with emission at 467 nm (green line) and 542 nm (red line). (b) Normalized excitation-dependent steady-state emission spectra of ***o*-Cz** masking at 2nd order Rayleigh with 5 nm slit width.

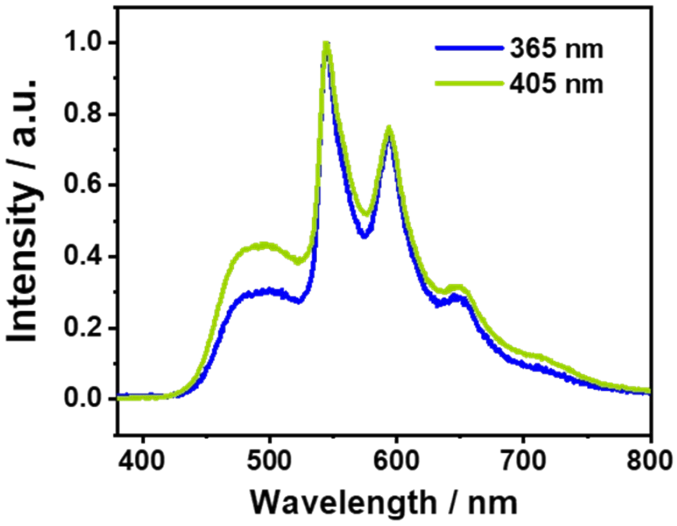

Figure S8. Phosphorescence spectra (delayed time = 8 ms) of ***o*-Cz** excited with different wavelengths in the crystalline state. The 365 nm and 405 nm were triggered with LED sources.

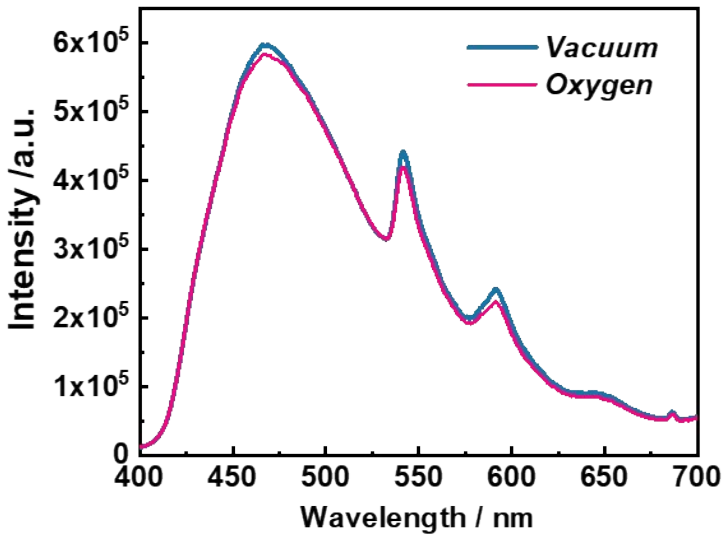

Figure S9. Steady-state PL spectra of ***o*-Cz** in vaccum (blue line) and oxygen (red line) conditions.

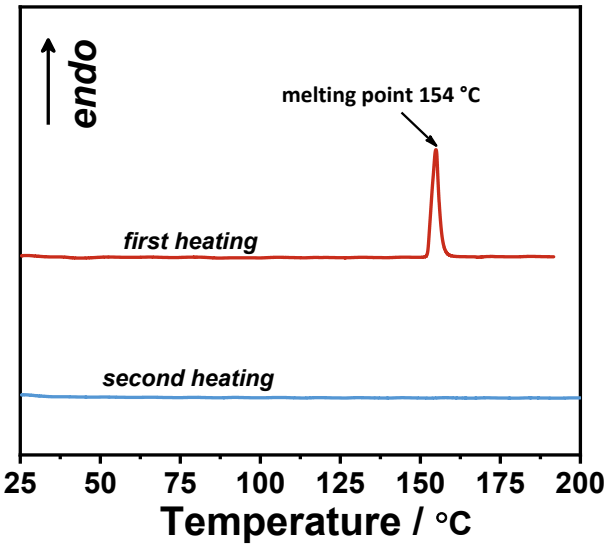

Figure S10. DSC curves of crystalline ***o*-Cz** on the first heating cycle (red line) and second heating cycle (blue line). The melting point is indicated.

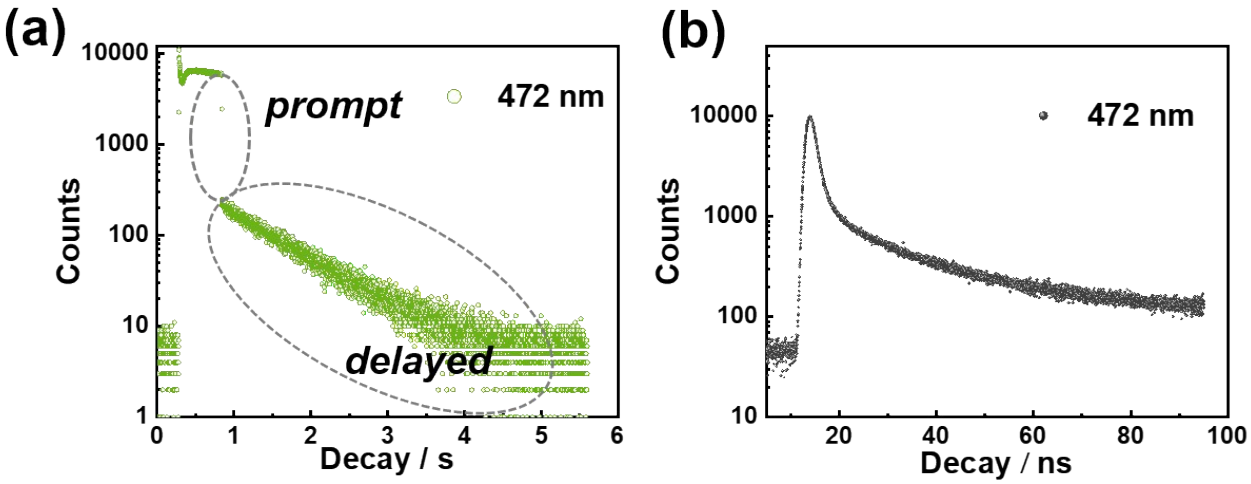

Figure S11. (a) The two-component decay curve of ***o*-Cz**. (b) The prompt decay at 472 nm.

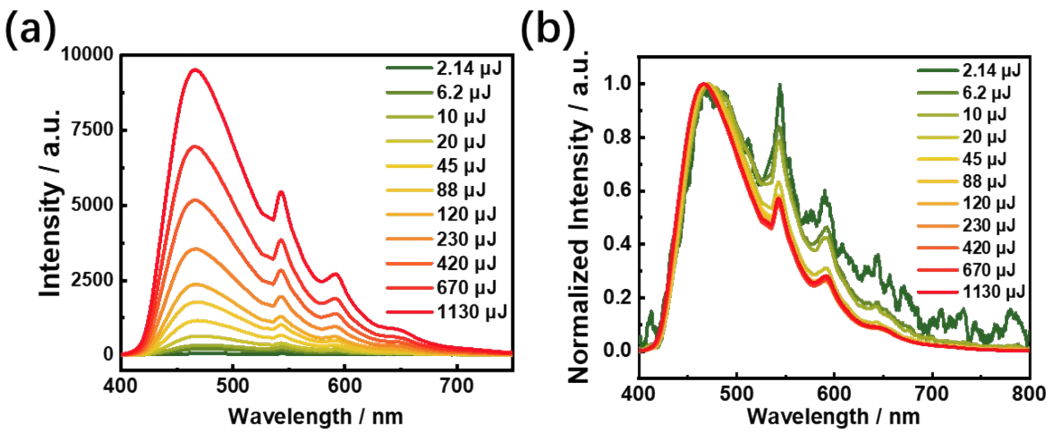

Figure S12. (a) Excitation energy-dependent steady-state photoluminescence spectra of ***o*-Cz** in the solid-state under ambient conditions masking at 532 nm (excited with 355 nm, YAG laser 15 Hz). (b) Normalized spectra profile.

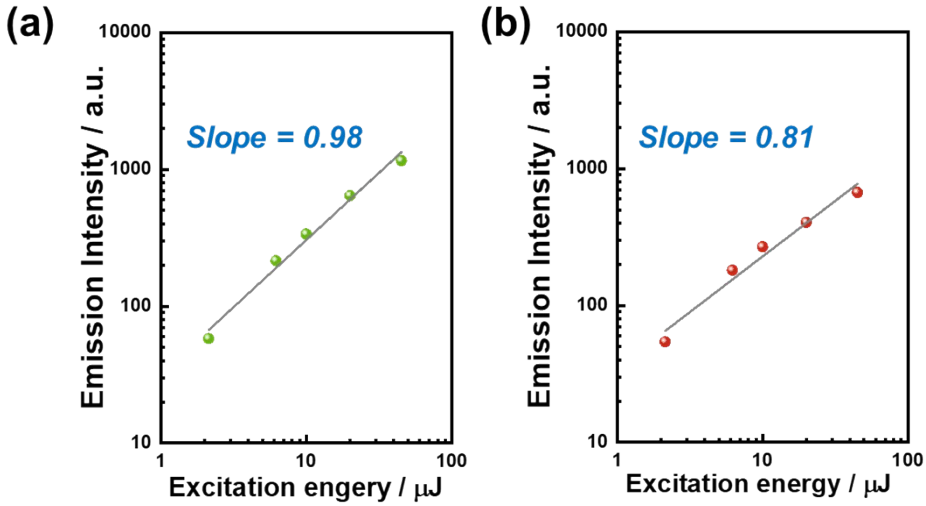

Figure S13. Variation of the emission intensity of ***o*-Cz** with increasing excitation energy in case of (a) collecting at 467 nm and (b) collecting at 542 nm. A clear linear dependence is observed at low input energy indicating the TADF process at 467 nm.

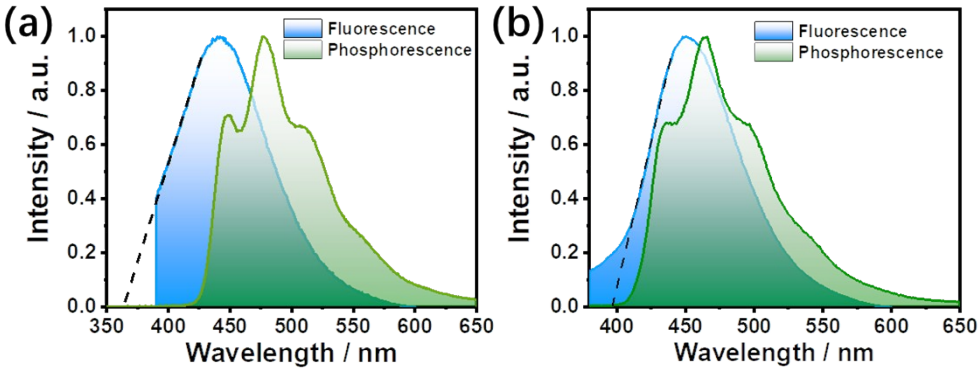

Figure S14. Fluorescence (room temperature, blue area) and phosphorescence (77 K, delay 8 ms, green area) spectra of (a) ***p*-Cz** and (b) ***o*-Cz** in THF solutions (1×10^{-5} M).

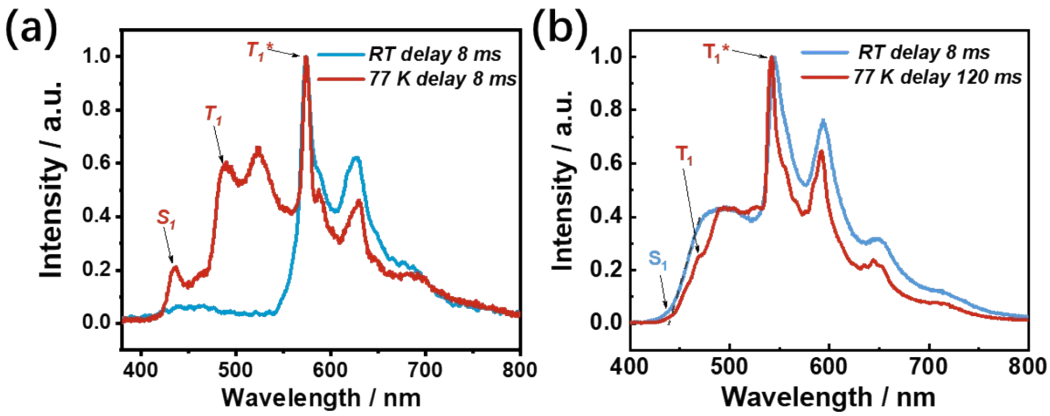

Figure S15. Delayed emission spectra of crystalline (a) ***p*-Cz** and (b) ***o*-Cz** at room temperature (blue line) and 77 K (red line). S_1 and T_1 represent the lowest singlet energy level and the lowest triplet energy level of ***o*-Cz** monomer, respectively. T^* represents the triplet energy level of the intermolecular electronic coupling dimer.

Table S2. Energy distribution of ***o*-Cz** in THF solution (1×10^{-5} M) and crystal by both theoretical and experimental calculation.

Energy / eV	in ***THF***		in ***Crystal***	
	Theoretical	Experimental	Theoretical	Experimental
S_1	2.97	3.14	3.22	2.82
T_1	2.77	2.86	3.01	2.65
ΔE_{ST}	0.20	0.28	0.21	0.17

Table S3. Energy distribution of ***p*-Cz** in THF solution (1×10^{-5} M) and crystal by both theoretical and experimental calculation.

Energy / eV	in ***THF***		in ***Crystal***	
	Theoretical	Experimental	Theoretical	Experimental
S_1	3.08	3.40	3.27	2.89
T_1	2.62	2.79	2.87	2.57
ΔE_{ST}	0.46	0.61	0.40	0.32

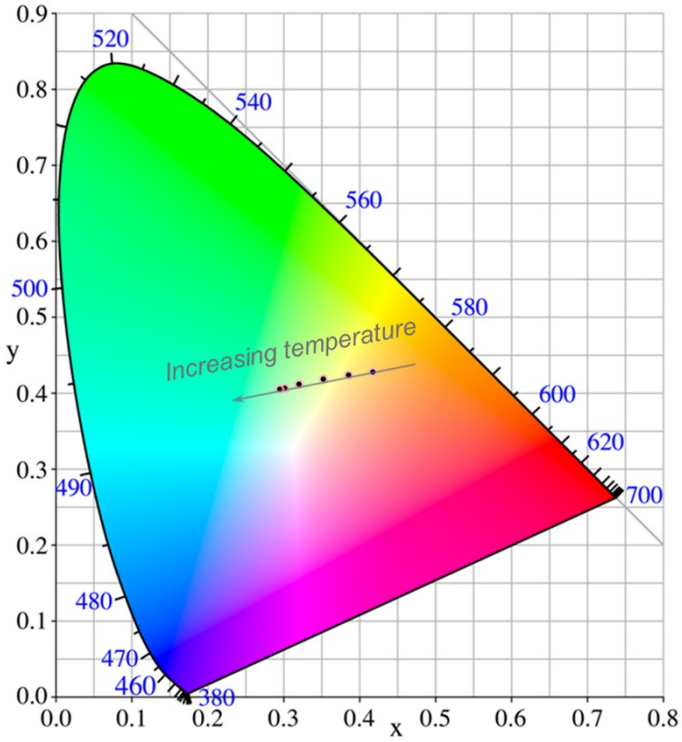

Figure S16. Temperature-dependent ultralong emission CIE coordinates of ***o*-Cz** under ambient conditions (excitation 405 nm, delay time = 8 ms).

Table S4. Temperature-dependent afterglow CIE coordinates of ***o*-Cz** under ambient conditions (excitation 405 nm, delay time = 8 ms)

Temperature / K	CIE / x	CIE / y
297	0.4161	0.4264
305	0.3853	0.4235
313	0.3520	0.4183
323	0.3199	0.4116
337	0.3017	0.4070
343	0.2943	0.4050

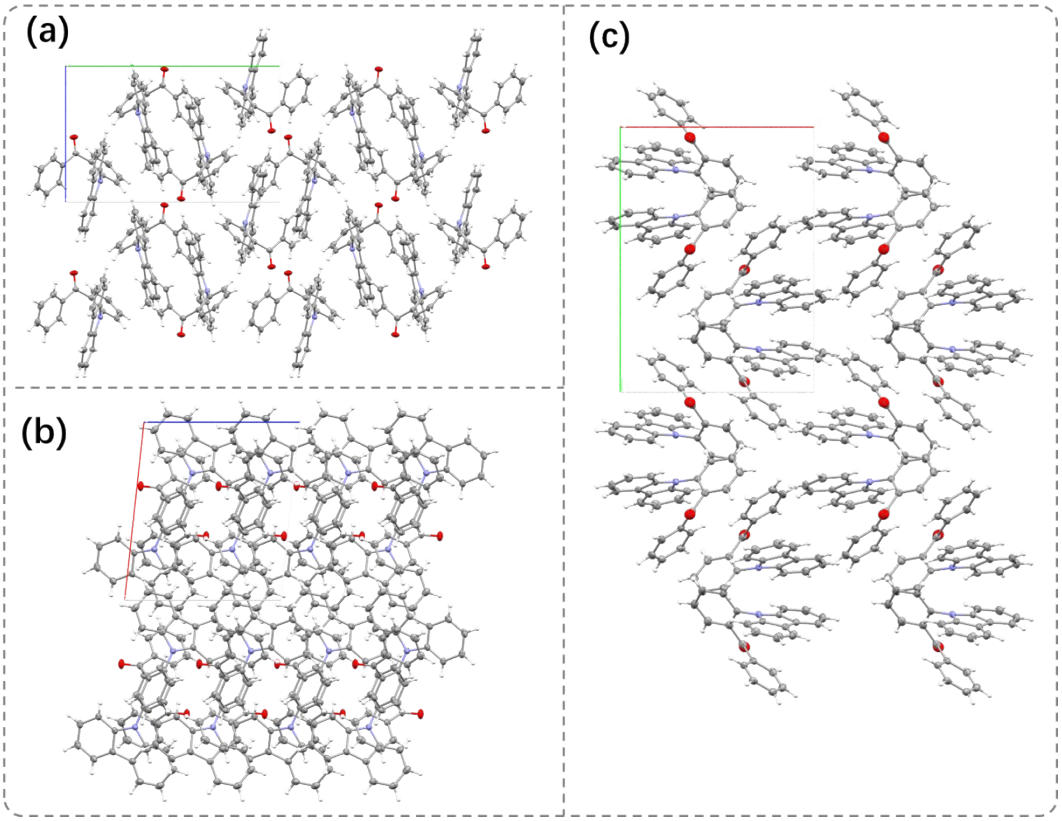

Figure S17. Molecular packing mode of ***o*-Cz** with a view from (a) an axis, (b) b axis and (c) c axis.

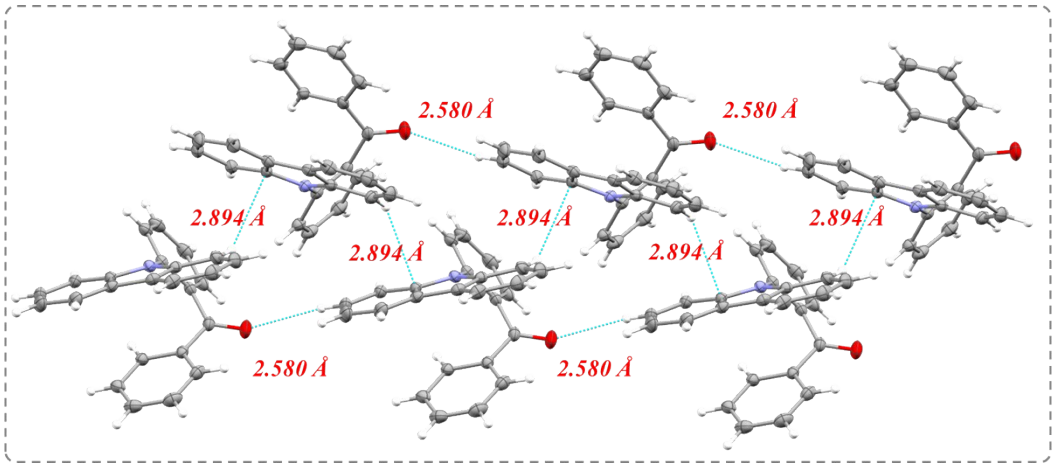

Figure S18. Molecular packing in the crystal lattice of ***o*-Cz**. The blue dotted lines represent intermolecular interactions of C=O···H and C-H···π.

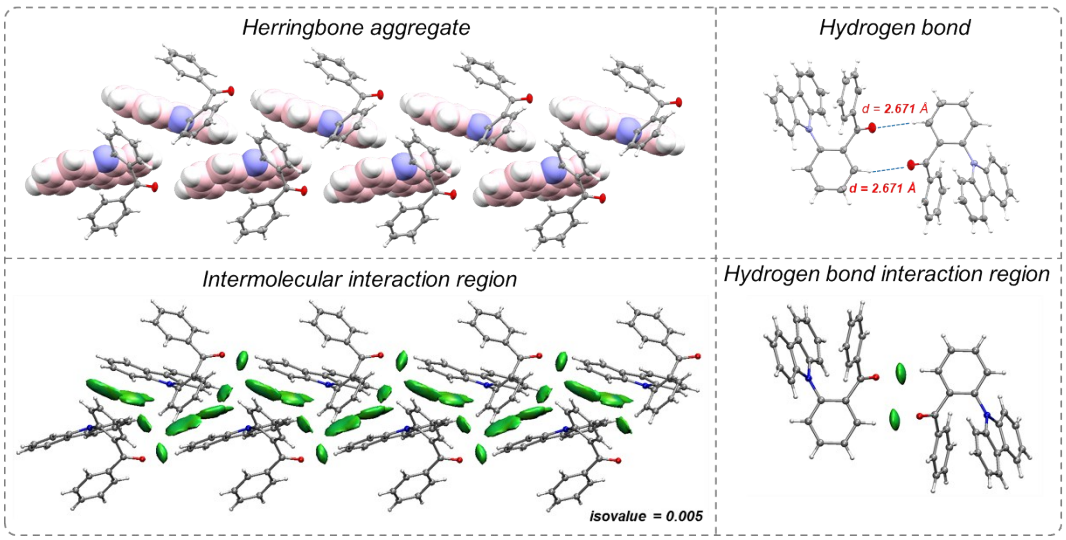

Figure S19. Herringbone aggregation and hydrogen bonds (upper) in the crystal lattice of ***o*-Cz**, and the visualization of corresponding interaction regions with an isovalue of 0.005.

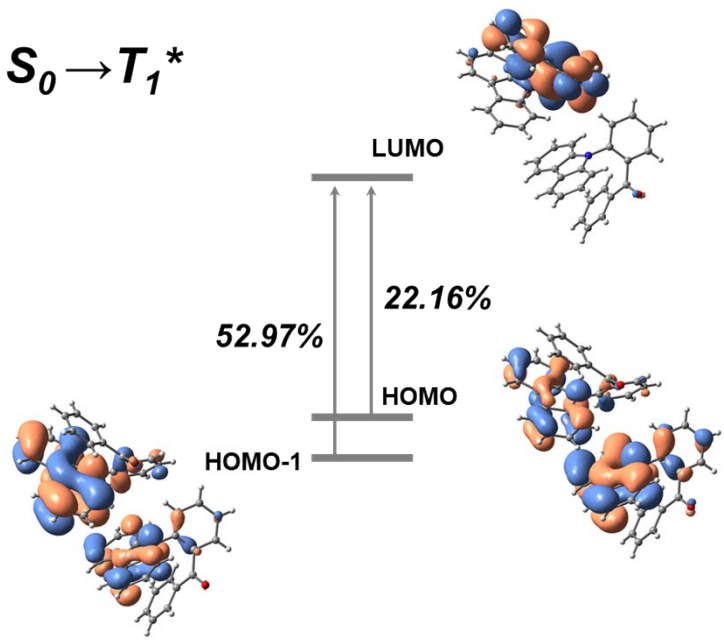

Figure S20. The intermolecular electronic coupling of the T_1* state in the herringbone dimer. The transition of the S_0-T_1* occurred between the herringbone dimer. T_1* represents the lowest triplet state of the dimer.

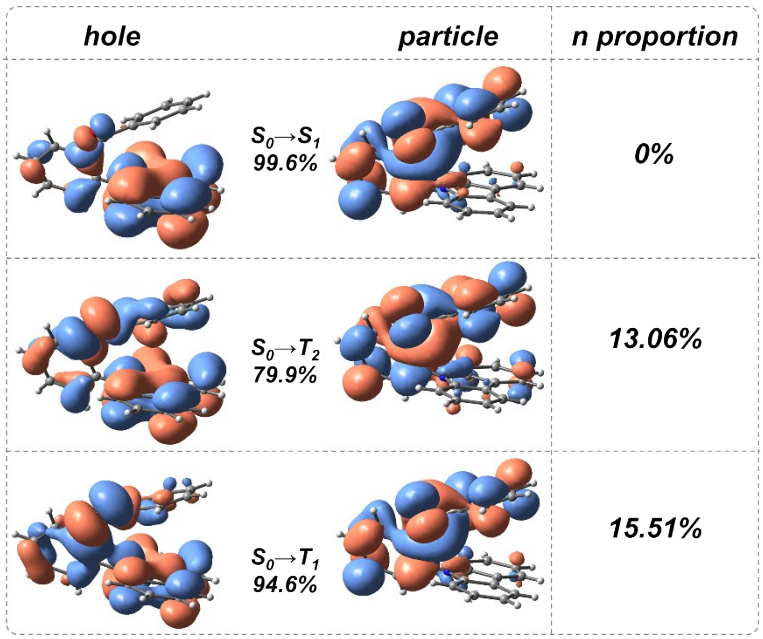

Figure S21. NTO distributions of S_1, lower-lying T_1, T_2 and T_3 at crystalline geometric structure of ***o*-Cz**. The n proportion represents the nπ^* configuration proportions of the corresponding excited states.

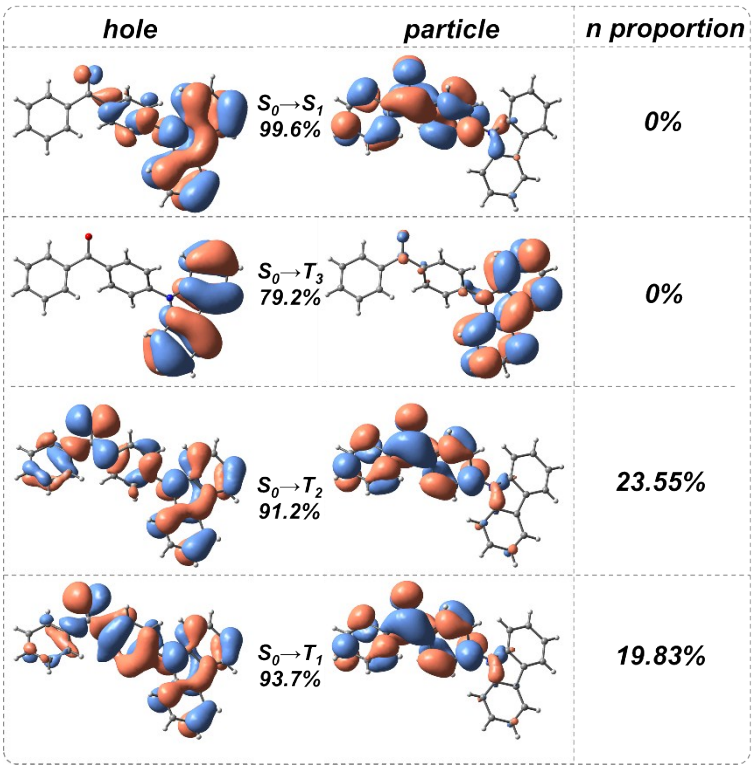

Figure S22. NTO distributions of S_1, lower-lying T_1, T_2 and T_3 at crystalline geometric structure of ***p*-Cz**. The n proportion represents the nπ^* configuration proportions of the corresponding excited states.

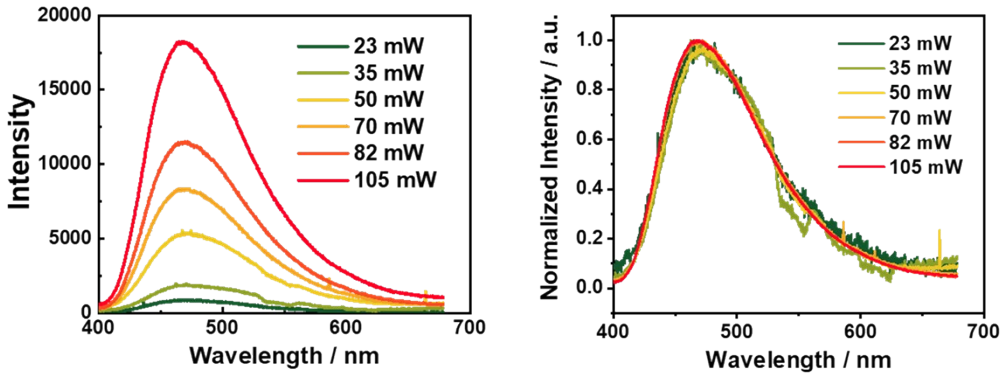

Figure S23. (a) Two-photon induced emission with varying input laser intensity; (b) Normalized emission profiles. The difference of the two-photon induced steady-state spectral profiles compared with the one-photon induced emission is due to the different spectrophotometers used.

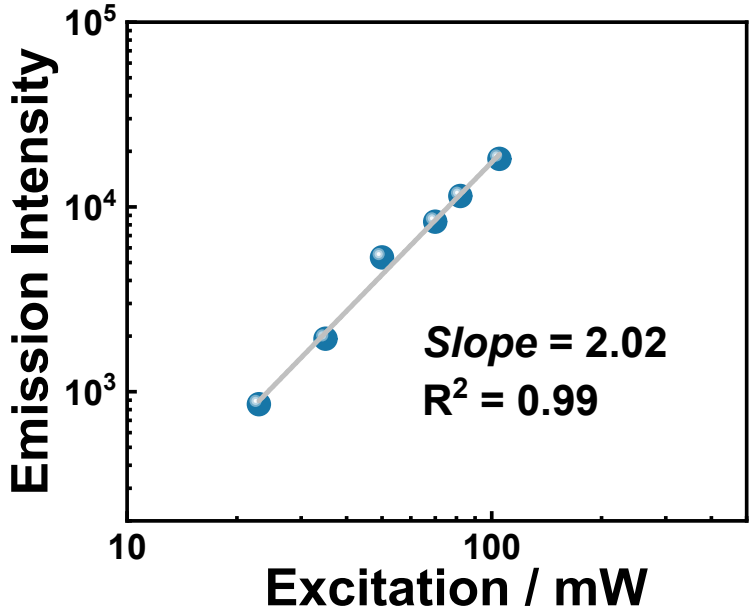

Figure S24. Variation of the emission intensity of **o-Cz** with increasing excitation energy triggered by a femtosecond laser (collected at 470 nm).

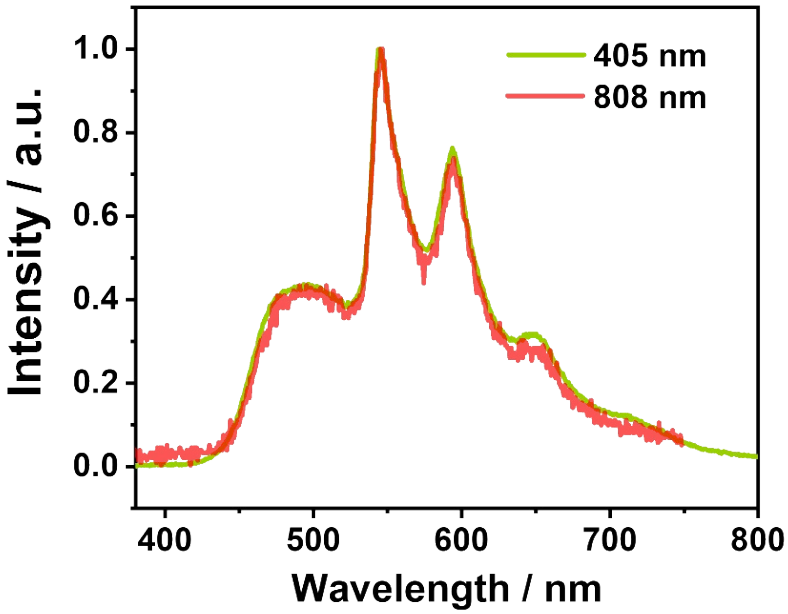

Figure S25. Phosphorescence spectra (delayed time = 8 ms) of ***o*-Cz** excited at different wavelengths in the crystalline state. The up-conversion excitation of 808 nm was triggered by a femtosecond laser and the 405 nm was triggered using an LED source. The 405 nm is nearly half of 808 nm.

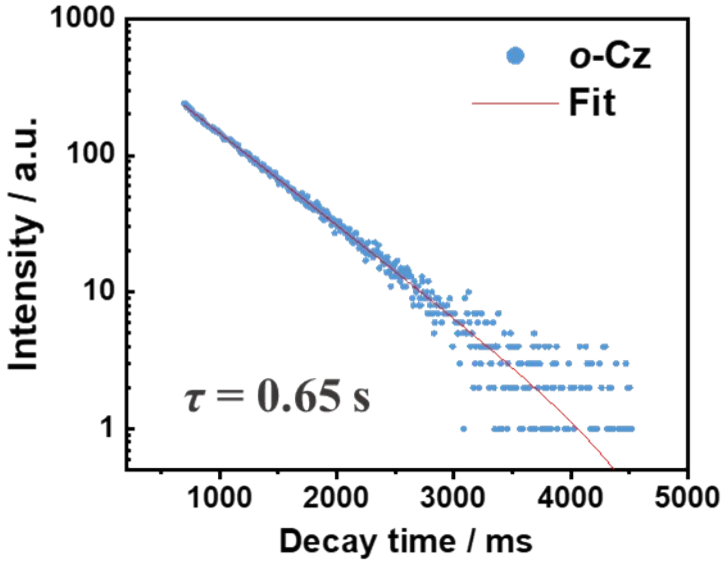

Figure S26. The decay curve of the ***o*-Cz** with the 808 nm laser excitation (collected at 542 nm). The shorten phosphorescence lifetime of the two-photon-excitation can be ascribed to the different spectrophotometers.

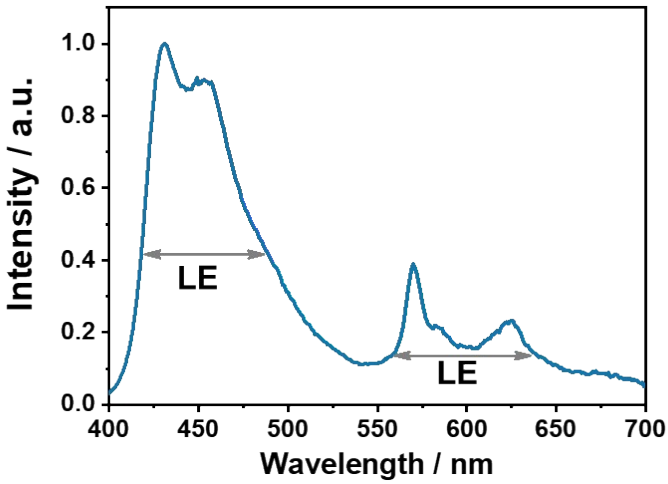

Figure S27. Steady spectrum of ***p*-Cz** in crystalline state.

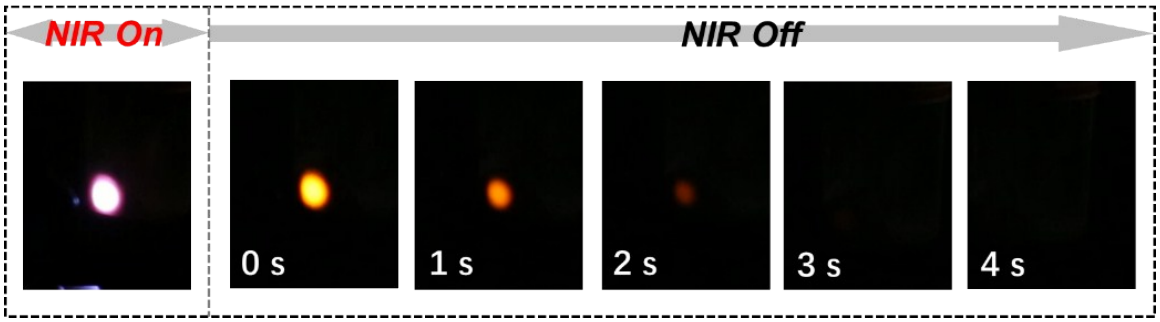

Figure S28. Photographs of ***p*-Cz** under NIR-light irradiation and after the light source has been switched off.

Structure information

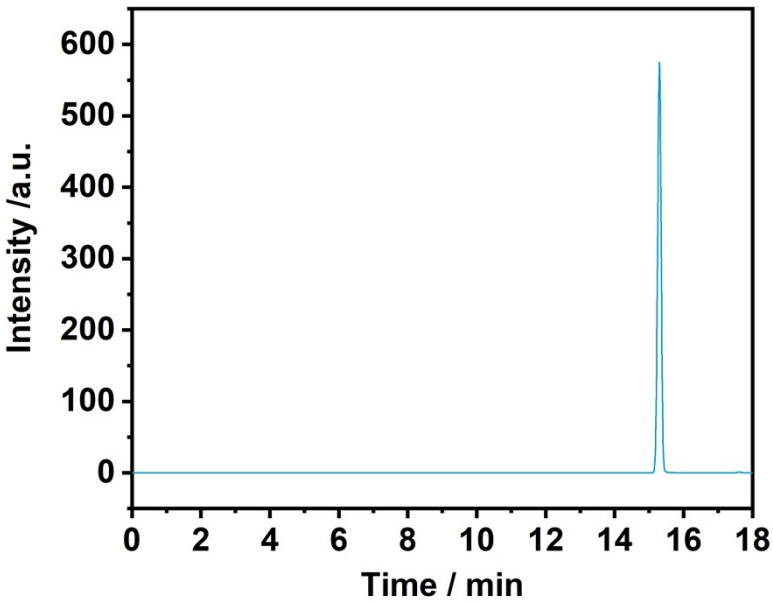

Figure S29. HPLC of ***o*-Cz** in acetonitrile solution (with a purity of 99.80%).

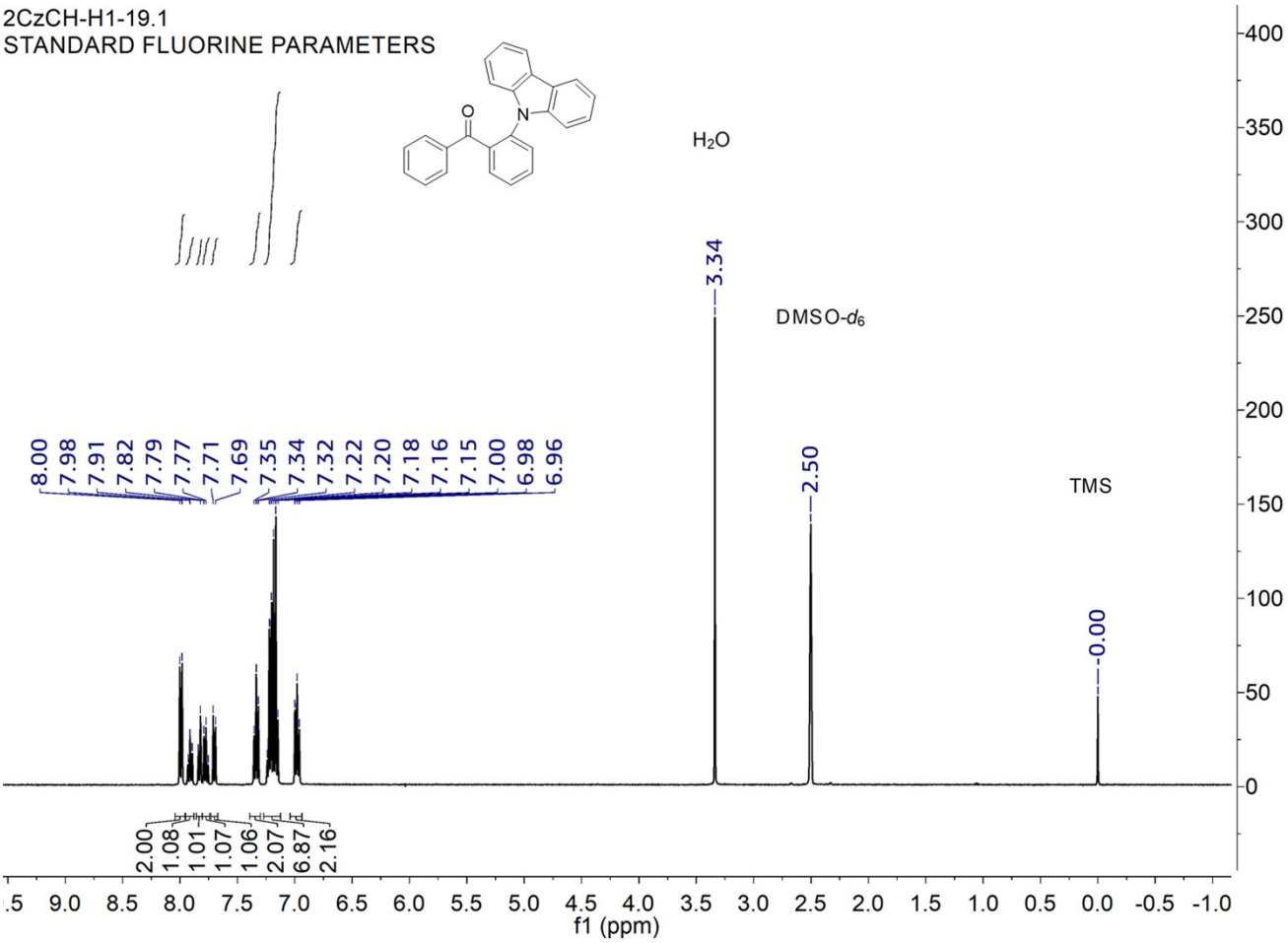

Figure S30. The ^{1}H NMR spectrum of ***o*-Cz** in DMSO-d_6.

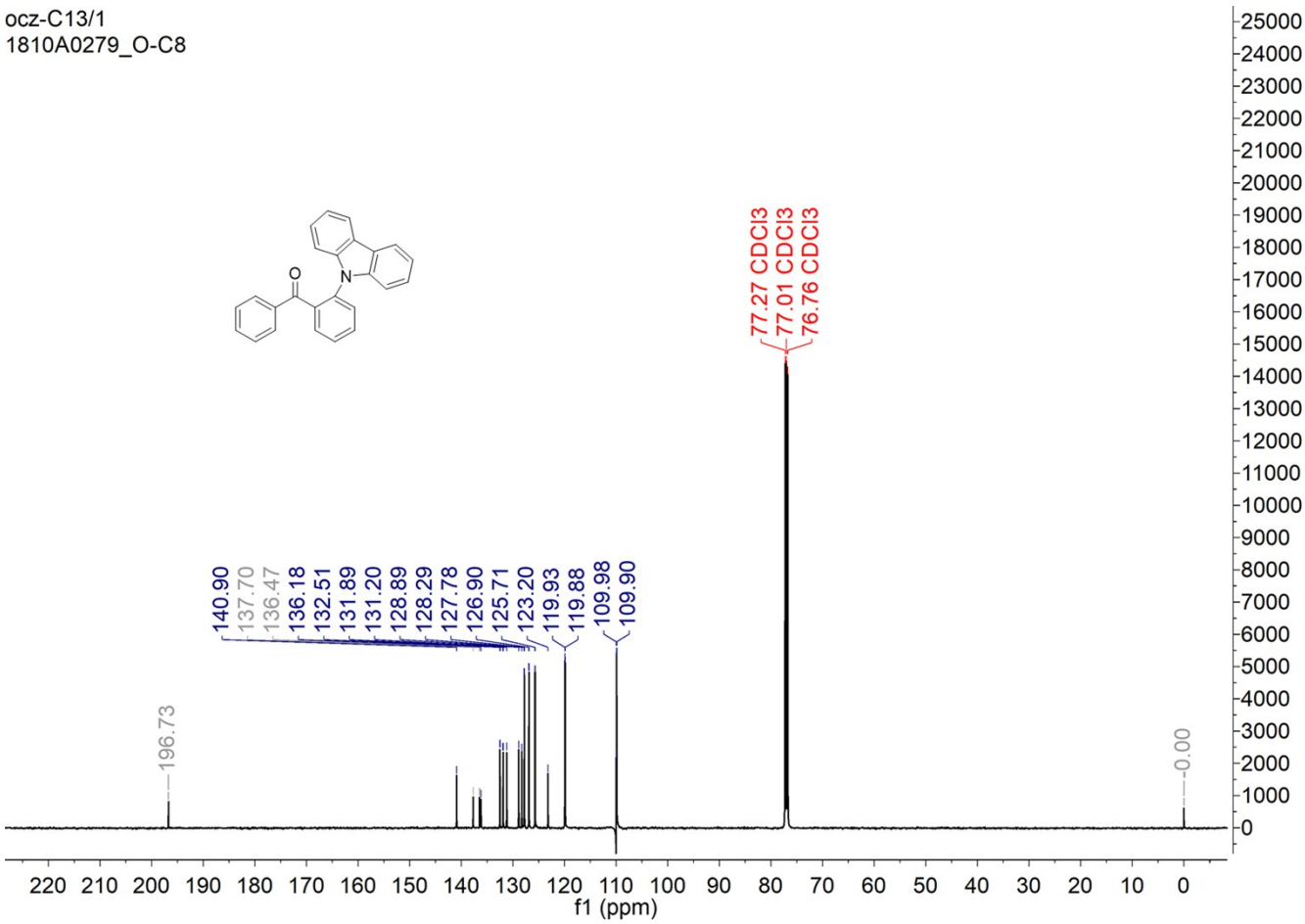

Figure S31. The ^{13}C NMR spectrum of ***o*-Cz** in $CDCl_3$.

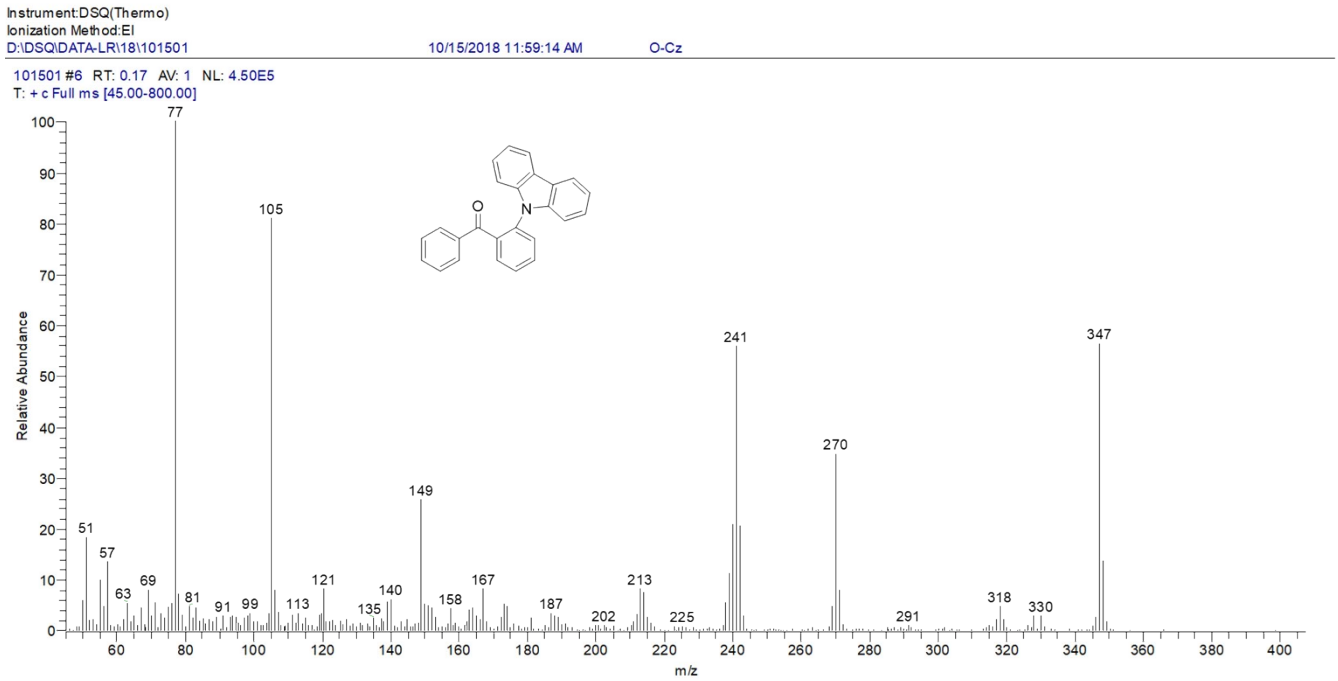

Figure S32. EI of ***o*-Cz**.

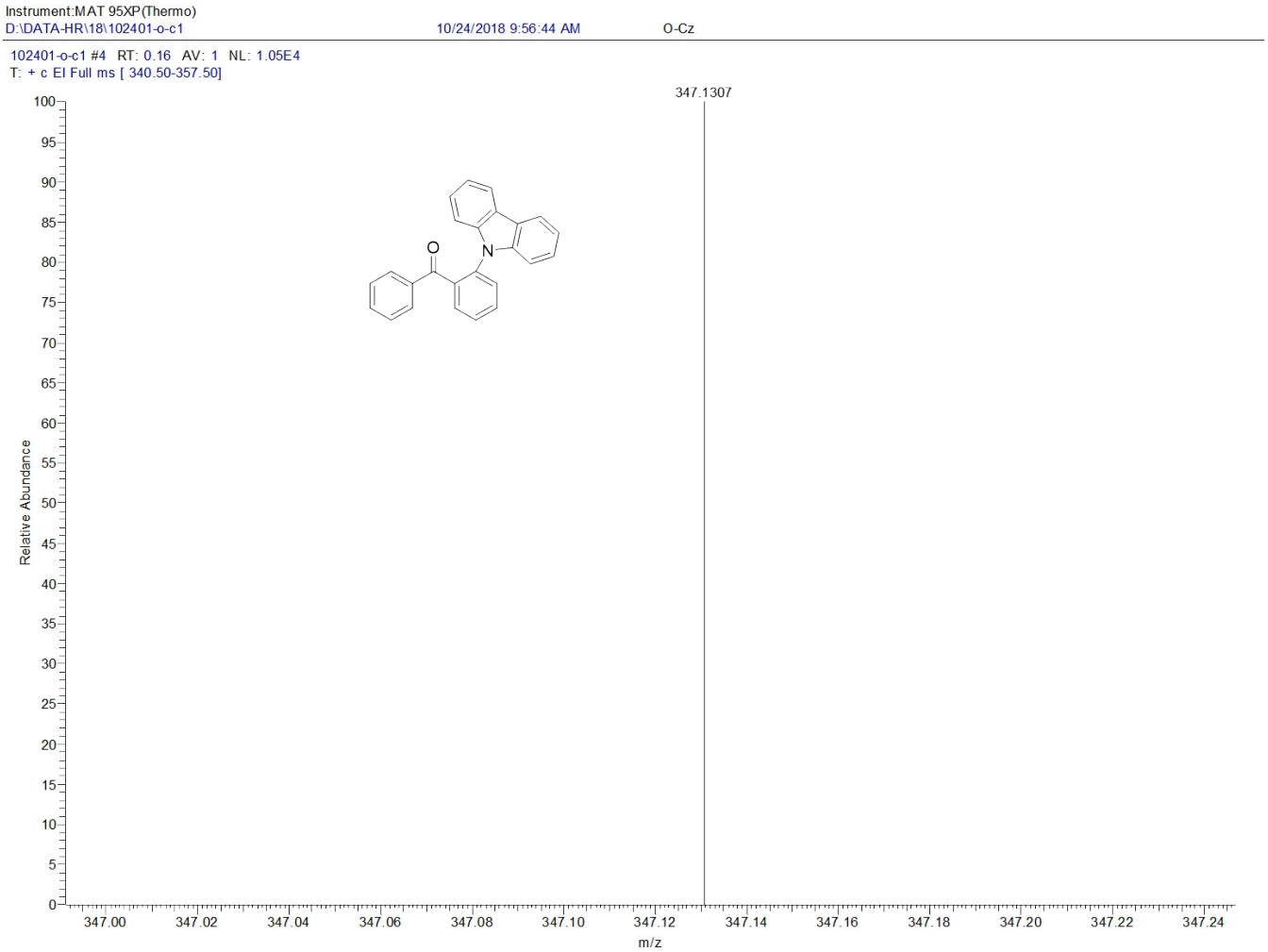

Figure S33. HRMS of ***o*-Cz**.

References

[1] Pu, X.; Qi, X.; Ready, J. M. *J. Am. Chem. Soc.,* **2009**, *131*, 10364–10365.
[2] Becke, A. D. *J. Chem. Phys.* **1993**, *98*, 5648–5652.
[3] Lee, C.; Yang, W.; Parr, R. G. *Phys. Rev. B*, **1988**, *37*, 785–789.
[4] Liu, W.; Wang, F.; Li, L. *J. Theor. Comput. Chem.,* **2003**, *02*, 257–272.
[5] Lu, T.; Chen, F. *J. Comput. Chem.,* **2012**, *33*, 580–592.
[6] (a) Johnson, E. R.; Keinan, S.; Sanchez, P. M.; Garcıa, J. C.; Cohen, A. J.; Yang, W. *J. Am. Chem. Soc.* **2010**, *132*, 6498–6506; (b) Lefebvre, C.; Rubez, G.; Khartabil, H.; Boisson, J. C.; Garcia, J. C.; Henon, E. *Phys. Chem. Chem. Phys.,* **2017**, *19*, 17928–17936.
[7] Humphrey, W.; Dalke, A.; Schulten, K. *J. Mole. Graph.,* **1996**, *14*, 33–38.
[8] Caylor, C. L.; Dobrianow, I.; Kimmr, C.; Thome, R. E.; Zipfel, W.; Webb, W. W. *Phys. Rev. E,* **1999**, *59*, 3831–3834.
[9] Orr, B. J.; Ward, J. F. *Mol. Phys.,* **1971**, *20*, 513–526.